Long-range chemical orders in Au–Pd nanoparticles revealed by aberration-corrected electron microscopy

Jaysen Nelayah, Nhat Tai Nguyen, Damien Alloyeau, Guillaume Yangshu Wang, Christian Ricolleau

Long-range chemical orders in Au-Pd nanoparticles revealed by aberration-corrected electron microscopy†

Jaysen Nelayah, Nhat Tai Nguyen, Damien Alloyeau, Guillaume Yangshu Wang and Christian Ricolleau

Received Xth XXXXXXXXXX 20XX, Accepted Xth XXXXXXXXX 20XX
First published on the web Xth XXXXXXXXXX 200X
DOI: 10.1039/b000000x

Despite the importance of gold-palladium nanoalloys in heterogeneous catalysis, the phase stability of Au-Pd alloy still remains unclear. We report here on the alloying and chemical ordering in epitaxially-grown and post-annealed gold-palladium nanoparticles (NPs) using aberration-corrected transmission electron microscopy. Au-Pd NPs with controlled size, composition and structure, were grown by pulsed laser deposition on freshly-cleaved NaCl(001) single crystals heated at 300°C. After transfer to an amorphous carbon support, the NPs were annealed in vacuum at elevated temperatures above 400°C for few hours (6-10 hours) to promote chemical ordering. The as-grown NPs were mostly monocrystalline with a chemically-disordered face-centered cubic structure. Upon high-temperature annealing, high degree of chemical ordering was observed in nanometer-sized NPs. Electron microscopy measurements showed that both $L1_0$ and $L1_2$ orders are stabilized in the Au-rich region of Au-Pd phase diagram. These ordered phases exist at temperatures as high as 600°C. Moreover, compositional analysis of single annealed particles revealed that the observed chemical ordering occurs in parallel to a two-tiered Ostwald ripening process. Due to this ripening process, a clear dependence between chemical composition and particle size is established during annealing with an enrichment in Pd as the NPs grow in size. Our results, besides clarifying some controversial aspects about long-range order in Au-Pd alloy, sheds light on the structural stability of Au-Pd nanoalloys at elevated temperatures.

1 Introduction

Gold-based bimetallic nanoparticles (NPs) are presently at the center of much scientific and technological interests due to their unique thermodynamic, optical and catalytic properties. In the field of heterogenous catalysis, among the wide range of gold-based bimetallic alloys, gold-palladium NPs have been widely studied. This is due primarily to Au-Pd alloys being an active catalysts in various reactions (in the synthesis of vinyl acetate monomer[1], selective oxidation of primary carbon-hydrogen bonds in Toluene[2], oxidation of primary alcohols to aldehydes[3], direct synthesis of hydrogen peroxide by reacting molecular hydrogen and molecular oxygen at ambient temperature[4]). In these reactions, Au-Pd NPs exhibit enhanced activity, selectivity and stability when compared to either pure Pd or Au nanocatalysts. The promotion of the catalytic properties in nanoalloys is explained on the basis of an enhancement of both electronic (ligands effects) and geometric properties (ensemble effects) upon intermetallic mixing[5]. In Au-Pd nanostructures, the ensemble effect is often assigned to a dilution of Pd surface atoms by gold. For instance, in the oxidation of glycerol to glyceric acid, a high activity and selectivity is associated with isolated Pd monomer sites in contact with Au atoms[6]. For the rational design of Au-Pd nanocatalysts, chemical and physical approaches have been developed. Chemical approaches involving colloidal synthesis methods (such as co-reduction and seeded-growth approaches) have yielded both completely random alloys[7,8] and core-shell structures[9]. Production of bimetallic Au-Pd nanoparticles/clusters has also been achieved by vapor deposition methods[10,11].

Information about chemical order and phase stability in Au-Pd alloy have been compiled by Okamoto and Massalski[12]. According to the experimental bulk phase diagram, Au and Pd show complete miscibility at all compositions in the solid phase. The resulting solid solution displays a random mixing arrangement with a disordered face-centered cubic (fcc) structure. In the fcc lattice, each atomic site is occupied by either a gold or palladium atom. The occupation probability of a given site depends on the ratio of the constituent elements. The most surprising features of this phase diagram is the presence of $L1_0$- and $L1_2$-types long-range ordered phases around compositions AuPd($L1_0$), Au_3Pd($L1_2$), and $AuPd_3$($L1_2$) despite that no chemical order has ever been observed experimentally in bulk Au-Pd. Inclusion of ordered phases in the bulk phase diagram is based on the assessment, by electron diffraction anal-

† Electronic Supplementary Information (ESI) available: [details of any supplementary information available should be included here]. See DOI: 10.1039/b000000x/

Laboratoire de Matériaux et Phénomènes Quantiques, Bâtiment Condorcet, CNRS UMR 7162,Université Paris Diderot, Paris, France. Fax: 01 5727 6241; Tel: 01 5727 6998; E-mail: jaysen.nelayah@univ-paris-diderot.fr

ysis, of the atomic structure of Au-Pd thin films evaporated on cleaved surfaces of KCl and NaCl salts and post-annealed at high temperatures[13–16]. Around compositions 25 and 75 atomic per cent (at.%) Au, a $L1_2$-type ordered structures have been experimentally observed with order-disorder (O/D) transition temperatures estimated at 850°C at $Au_{0.8}Pd_{0.2}$ [14,16] and between 780 and 900°C at $Au_{0.2}Pd_{0.8}$ composition[15]. Around the equiatomic composition, a $L1_0$-type order was identified by Nagasawa in thin AuPd film annealed at 500°C during 4 hours[13]. The corresponding O/D transition was observed between 650 and 700°C. The $L1_0$ structure is based on a tetragonal lattice characterized by planes of pure Au atoms and pure Pd atoms alternately stacked along the c-axis of the tetragonal unit cell. As for the $L1_2$ order, it occurs on a fcc lattice with either Au (in $AuPd_3$) or Pd (in Au_3Pd) occupying the corners of the cube and the other element centered on the six faces of the cubic unit cell. The unit cells (Fig. 1S) and space groups of the fcc, $L1_0$ and $L1_2$ structures are included in the Electronic Supplementary Information (ESI). It should be noted that the existence of this $L1_0$ phase is still uncertain. Firstly, in a later paper[14], Nagasawa questioned the reliability of his experiments showing the existence of $L1_0$ phase. Secondly, based on short-range order parameter measurements in Au-Pd alloys, the temperature range of stability of the $L1_0$ order is expected to be lower than 100°C[17]. Recently, a $L1_1$ order has been observed experimentally in core-shell NPs with a Au octahedron core and a Pd epitaxial shell heat-treated at 250°C [18]. This $L1_1$ order was limited to the interfacial region between the core and the shell and was assigned to the diffusion of Au atoms from the core to the shell so as to release interface mismatch. In this study, no other chemical order phase was identified.

Gaining deeper insights into the phase stability of Au-Pd alloys has also relied intensively on atomistic simulations. The equilibrium configurations of Au-Pd alloys have been studied by Monte Carlo simulations using embedded-atom method interatomic potentials[19,20] and Density Functional Theory calculations combined with cluster expansion method[21,22]. At equiatomic composition, the low-temperature ordered phases derived from first-principles cluster expansion methods, by Barabash *et al.*[21] and Sluiter *et al.*[22], predict bulk AuPd to be stable in chalcopyritelite Au_2Pd_2 superlattice structure[23,24]. In comparison, Monte Carlo simulations predict the existence of $L1_0$ and $L1_2$ orders in both Au-Pd bulk alloy and nanoalloys (consisting of about 1000 atoms or less) with cuboctahedral, truncated octahedral and spherical shapes[19]. In these nanoalloys, chemical order is predicted in the core alongside systematic surface and sub-surface enrichments in Au and Pd respectively. In bulk AuPd alloy, the $L1_0$ order is calculated below 100°C. As observed experimentally in CoPt nanoclusters[25], a depression of the O/D temperature is expected in nanoclusters.

Developing new Au-Pd catalysts or enhancing the performances of existing ones on a rational basis would gain significantly from a clear knowledge of the phase diagram of Au-Pd NPs. Due to the scarcity and reliability of existing experimental and calculation data, the existence of chemical order in Au-Pd alloy is still a highly debating issue. In this paper, through the fabrication of Au-Pd nanoalloys and study of their structure by aberration-corrected transmission electron microscopy (TEM), long-range orders have been unambiguously identified in Au-Pd alloy. These results constitute a major step towards a complete understanding of the phase stability of Au-Pd alloy.

2 Experimental conditions

Gold-palladium NPs were synthesized by pulsed laser deposition (PLD) technique in a high vacuum chamber under a pressure of about 10^{-7} Torr[26]. The Au-Pd NPs were deposited on a 1×1 cm^2 freshly cleaved sodium chloride NaCl(001) single-crystal surface. To ensure well-oriented growth of the NPs on the substrate, the latter was heated at 300°C during deposition. Real-time monitoring of the temperature was achieved using Eurotherm controller and K-type thermocouple. The transfer of material from the target to the substrate was done by using a KrF excimer laser with wavelength of 248 nm with pulse duration of 25 ns and a repetition rate of 5 Hz (COMPexPro 102 F, COHERENT®). Owing to the ablation thresholds of Au and Pd, the pulse energy at the exit of the laser was set in the range 250-400 mJ. To fabricate Au-Pd nanoalloys, two ultra pure (99.99% purity) Au and Pd targets were alternately ablated. To ensure complete mixing of the constituent atoms, the deposition was divided in sequences. In each sequence, the total thickness of deposited metals was fixed to 1 Å. The deposition rate for each metal was controlled by an *in situ* quartz balance prior to deposition. As the constituent metals can be mixed in any ratio, our set-up enabled a precise control of both the composition and nominal thickness of alloy deposited (which corresponds to the total thickness of metals deposited in a continuous film approximation). In the present study, the nominal thickness deposited was fixed to 1 nm to ensure the formation of well-separated NPs with sizes of the order of a few nm. After deposition, the Au-Pd NPs were covered by a few nm-thick amorphous (a-)carbon film obtained by ablating a pure carbon target present in the same set-up. Carbon replica was obtained by dissolving the sodium chloride in desionized water followed by the transfer of the carbon-supported NPs to standard copper TEM grids (holey carbon on a 400 mesh Cu grid, Agar Scientific) for post-annealing experiments and structural investigations by transmission electron microscopy (TEM). More information about the preparation of carbon replica can be found in[27]. Prior to annealing and TEM analysis, the replicas were covered by another thin film of a-carbon to limit oxidation of the

bimetallic NPs when the grids are exposed to air and sintering of NPs during thermal annealing at high temperatures. Post-annealing of the a-carbon supported NPs was done at temperatures between 400 to 600°C for different time intervals. Annealing experiments were undertaken in the growth chamber using the same heating stage as the one used to heat the rock salt substrate during deposition. After annealing, the specimen was quenched to room temperature in vacuum. The pressure in the chamber during annealing was kept around 10^{-7} Torr. The structure of the as-grown and annealed NPs was studied by standard and aberration-corrected TEM at 200 kV. Low magnification imaging, selected-area electron diffraction (SAED) and energy dispersive X-ray spectroscopy on NP assemblies (TEM-EDS) were undertaken in a JEOL 2010 TEM. **All SAED patterns are obtained by selecting nanoparticles distributed over circular area with a diameter of about 560 nm**. For ultra-high resolution TEM (UHRTEM) imaging and single-particle X-ray analysis in scanning mode (STEM-EDS), a JEOL ARM 200F microscope was used. This microscope combines a newly-developed cold field emission gun[28] and a CEOS hexapole spherical aberration corrector (CEOS GMBH)[29] to compensate for the spherical aberration of the objective lens. This unique TEM configuration achieves a point resolution of 75 pm at 200 kV[30]. **High resolution images have been acquired with negative Cs values up to -500 nm and with the objective lens slightly overfocused. In these conditions, the image contrast due to the carbon matrix is minimized allowing particle imaging with high signal-to-noise ratio and atomic columns appear in white at the Scherzer defocus.** STEM-EDS spectra were obtained with acquisition times of 50 or 100 s. A typical raw STEM-EDS spectrum is shown in Fig. 2S. Particle composition was determined by analyzing the intensities under the Au-$M_{\alpha,\beta}$ (between 2.00 and 2.24 keV) and Pd-$L_{\alpha,\beta}$ (between 2.70 and 2.94 keV) edges using the Cliff-Lorimer method[31]. The Cliff-Lorimer K factor used for quantification was experimentally determined by utilizing a thin wedge-shapes $Au_{48}Pd_{52}$ film fabricated by PLD and thinned by focused ion beam milling. The composition of the film was precisely determined by inductively coupled plasma optical emission spectrometry prior to thinning. Instead of using a fixed probe, the electron beam was continuously scanned in a controlled manner over a rectangular region on the NPs during STEM-EDS measurements so as to minimize electron beam induced damage and ensure that the measured composition is as close as possible to the real one. For each particle, the scanned region was chosen to encompass as much as possible its projected area.

3 Results

3.1 Structure of faceted Au-Pd NPs observed by selected area electron diffraction and ultra high resolution transmission electron microscopy imaging

Au-Pd nanoparticles with composition between $AuPd_3$ and Au_3Pd were fabricated. A low magnification bright field TEM image of an assembly of as-grown NPs on the a-carbon support is shown in Fig. 1. The NPs display mostly square or rectangular outlines. The average projected area diameter, i.e. the diameter of a perfect circle enclosing an area equivalent to the projection area of the NP, follows a narrow distribution with a mean diameter of 4.8 nm (see inset of Fig. 1a). According to TEM-EDS measurements (data not shown here), the mean composition of the present specimen is 60±5 at.% Au (using the X-ray detector fitted to the JEOL 2010 TEM). The SAED pattern, obtained from the assembly of NPs in the TEM image, is shown in Fig. 1b. It should be noted that all diffraction patterns presented in this work were acquired on NPs with sizes under 20 nm. The SAED pattern of the as-grown NPs is composed of well-defined diffraction spots. This single crystal-like electron diffraction pattern indicates the presence of well-oriented Au-Pd NPs on the carbon replica. The production of well-oriented NPs is a result of the epitaxial growth of the bimetallic nanoparticles on the rock salt substrate. The predominant epitaxial relationship between the metals and the salt substrate is most likely the cube-on-cube orientation epitaxy (100)Au-Pd‖(100)NaCl, [001]Au-Pd‖[001]NaCl as previously observed in epitaxially-grown Pd NPs on NaCl(001) [32–35]. The relative orientation of the fabricated NPs is preserved during the preparation of carbon replica. Indexing the SAED pattern shows that it is composed of sharp and intense 200 and 220 fundamental reflections. These reflections are assigned to the presence of completely alloyed Au-Pd NPs having disordered fcc structure and oriented such as one of the axes of their cubic lattice are perpendicular to the support.

The as-grown NPs were also imaged by ultra-high resolution TEM (UHRTEM). Fig. 1c shows UHRTEM images of two as-grown NP in <001> orientation alongside the corresponding Fourier transforms (FT). The FT patterns show the 200 and 220 spots of the fcc structure. Both NPs are faceted single crystal with main edges and minor truncations parallel to the <110> and <100> directions respectively. As previously observed in Pd NPs evaporated on NaCl at 150°C[32], the shape of the Au-Pd NPs, dictated by the growth kinetics, is most probably a truncated octahedron. In the <001> orientation, the latter appears as a square/rectangle. In addition to single crystals, a few polycristalline fcc NPs are also observed. Their average size exceeds 10 nm. NPs with structure (composition, atomic arrangement) comparable to those presented in Fig. 1 were subjected to long high-temperature annealing

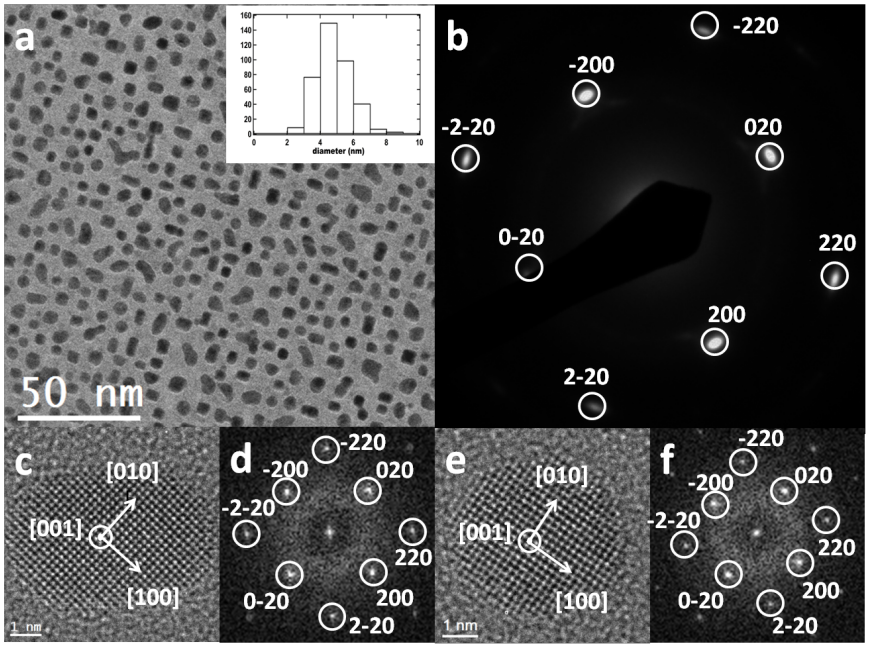

Fig. 1 (a) Low-magnification TEM image of carbon-supported Au-Pd nanoparticles (NPs) consisting of about 60 at.% Au. Prior to the transfer to the carbon support, the NPs were epitaxially grown, by pulse laser deposition, on a freshly cleaved NaCl(001) surface. In inset, the histogram of the size distribution of 386 NPs is shown. The average in-plane particle size is 4.8 ± 1.0 nm. In (b), the selected-area electron diffraction (SAED) pattern from the assembly of nanoparticles is presented. (c) and (d) UHRTEM images of two as-grown fcc NPs on the amorphous carbon support. The NPs are in close [001] orientation. The NPs are faceted single crystal with main edges parallel to the $<110>$ directions and minor truncations in the $<100>$ ones. The corresponding Fourier Transform (FT) patterns are also displayed alongside the corresponding UHRTEM images.

in vacuum. Structural changes that occur during annealing are described in the next section.

3.2 Atomic ordering observed by selected area electron diffraction and ultra high resolution transmission electron microscopy imaging

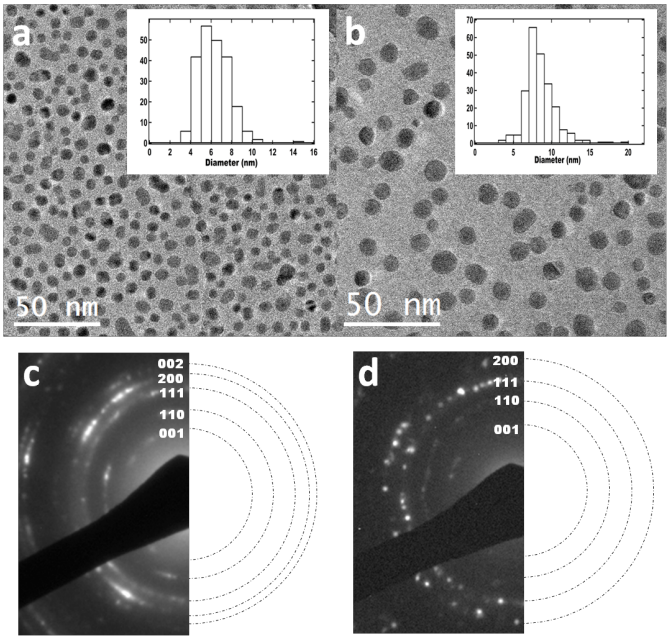

Fig. 2 (a) Low-magnification TEM images and the corresponding SAED patterns of two annealed specimen (samples A and B). Sample A consists of initially disordered fcc NPs, similar to those in Fig. 1, annealed at 600°C during 10 hours. Sample B consists of NPs with composition comparable to those in Fig. 1 annealed at 500°C during 8 hours. The size distribution of the two annealed samples are given in the insets of (a) and (b). The size distribution in (a) is constructed by analyzing the size of 240 NPs in sample A. The one shown in (b) is built from size distribution of 237 NPs from three different TEM images of sample B. (c) and (d) show SAED patterns obtained on samples A and B respectively. In (c), 001 and 110 superlattice reflections and a splitting of the 002 diffraction rings are visible.

TEM images and the corresponding SAED patterns of two annealed specimen (A and B) are shown in Fig. 2. Sample A (Fig. 2a) consists of NPs, similar to those in Fig. 1, annealed at about 600°C for 10 hours. Sample B (Fig. 2b) consists of NPs, with same composition as in Fig. 1, annealed at about 500°C for 8 hours. It should be noted that the as-grown NPs annealed in sample B had an average in-plane size double that of the NPs shown in Fig. 1a (comparison of the histograms in Fig. 1 and 3S). This explains the slightly larger in-plane size and lower surface coverage observed in sample B as compared to sample A. From the comparison of Fig. 1 and 2, two observations can be made about the influence of annealing. Firstly, a clear evolution of the nanoparticle's in-plane morphology of the NPs from square/rectangular to rounded profiles is observed upon annealing (Fig. 2a-b). Secondly, the mean in-plane size is increased during annealing in both samples. In sample A, analysis of 240 NPs from the TEM image in Fig. 2a gives a projected area diameter equals to 5.9 ± 1.9 nm (as compared to a mean in-plane size of 4.8 nm before annealing). Similarly, the in-plane diameter measured in sample B is 8.5 ± 2.1 nm as compared to 6.5 ± 2.2 nm before annealing (Fig. 3S). The SAED pattern of sample A is of powder-type (Fig. 2c). This results from the loss, during annealing, of the preferential $<001>$ orientation perpendicular to the support in the as-grown sample. On annealing at 600°C, we note in the SAED pattern (i) a splitting the 002 diffraction rings indicating a loss of the original cubic structure, (ii) the appearances of 001 and 110 superlattice reflections and (iii) the absence of the 100/010 superlattice reflection. The size distribution in annealed sample B is comparable to that observed in A (see insets of Fig. 2a-b for a comparison of the size distributions of the annealed NPs in A and B). The SAED pattern of the NPs in the TEM image shown in Fig. 2d shows 001 and 110 superlattice reflections indicating that chemical order is again present. But, no splitting of the 002 reflections appears here. The SAED results from both samples are consistent with the presence of chemical orders of either tetragonal $L1_0$-type or cubic $L1_2$-type. The splitting of the 002 diffraction rings observed in sample is a strong indication of the predominance of the $L1_0$ order in that case. To determine unambiguously the chemical orders that exist in samples A and B, the structure of the annealed NPs was studied on single particle level by UHRTEM imaging.

Fig. 3 shows UHRTEM images of chemically-ordered NPs from annealed samples A and B together with the corresponding FT images (below each UHRTEM image). These measurements show that the chemical order in sample A is predominantly of $L1_0$-type. Fig. 3a show a $L1_0$ NP imaged close to the [100] orientation. In this orientation, the tetragonal c-axis is in the plane of the carbon support. Analysis of the corresponding FT spectrum shows the presence of 001 superlattice reflections. In Fig. 3b-c, the $L1_0$-ordered NP is close to the [001] orientation, i.e. with its quadratic c-axis aligned normal to the carbon substrate. 110 superlattice reflections are clearly visible. The appearance of both the 001 and 110 superlattice reflections in the SAED pattern shown in Fig. 2c results from the presence of all three variants of the $L1_0$ phase in the annealed sample. These variants differ by the orientation of the c-axis of the tetragonal lattice with respect to the plane of the substrate. The value of the tetragonality ratio (c/a ratio) of the $L1_0$ order, deduced from the previously shown SAED data and UHRTEM images of NPs close to the [001]

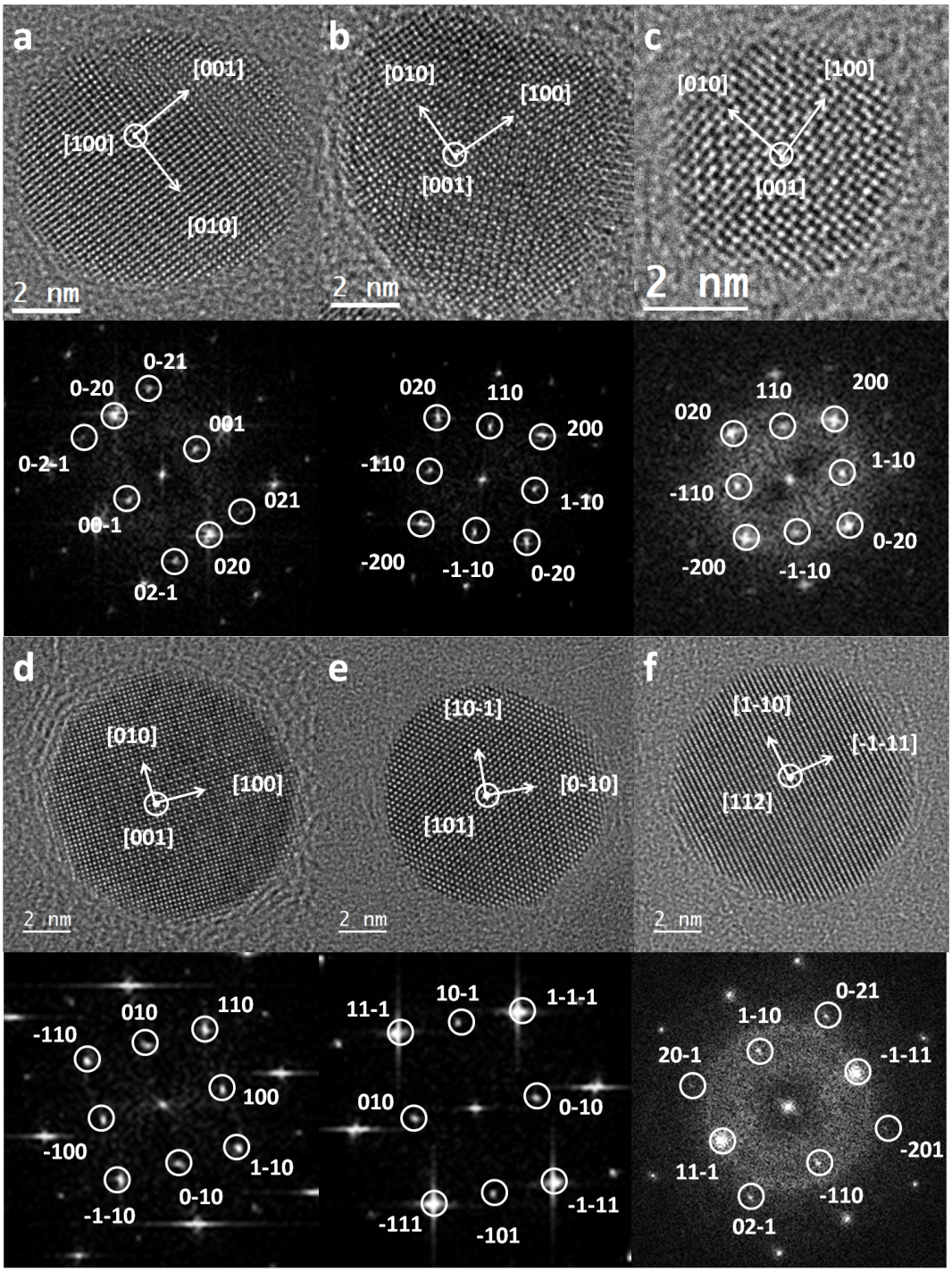

Fig. 3 UHRTEM images of $L1_0$ (a-c) and $L1_2$ (d-f) Au-Pd nanoparticles from samples A and B. The corresponding FT patterns are shown below each image. (a-c) $L1_0$-ordered NPs imaged close to the [100] (a) and [001] (b-c) directions. In those directions, chemical order is evidenced through the appearance of 001 and 110 superlattice reflections in the FT patterns. The $L1_2$ structures in (d-f) are in close [001], [101] and [112] orientations respectively. Again, strong superlattice reflections appear on the FT patterns.

orientation, is about 0.92. This value is very close to the one measured experimentally by Nagasawa in AuPd thin films (c/a = 0.93)[13]. In sample B, the ordered NPs are mostly of $L1_2$-type. Fig. 3d-f shows UHRTEM images of $L1_2$-ordered NPs from sample B. In Fig. 3d, the particle is image close to the [001] orientation. $L1_2$-order is evidenced by the presence of 100 and 110 superlattice reflections in the FT pattern. The NPs in Fig. 3e-f are imaged along the [101] and [112] orientations respectively. Again, 110 superlattice reflections are seen in the corresponding FT patterns. High-resolution measurements such as the one presented here show that the ordered NPs are mostly single crystals with truncations along the <110> and <100> directions. In comparison to as-grown NPs, truncations along the two sets of direction are equally favorable in the annealed NPs and result in their rounded morphologies. **Finally, it should be noted that the results present here are extracted from a systematic study of the thermal stability of Au-Pd nanoalloys as a function of annealing temperatures and durations. In this study, particle composition was between the $AuPd_3$ and Au_3Pd. Annealing temperature was set between 500 and 700°C for duration up to 24 hours. Our annealing experiments showed that no chemical order is stabilized when the annealing time was less than 6 hours irrespective of particle composition and annealing temperature**

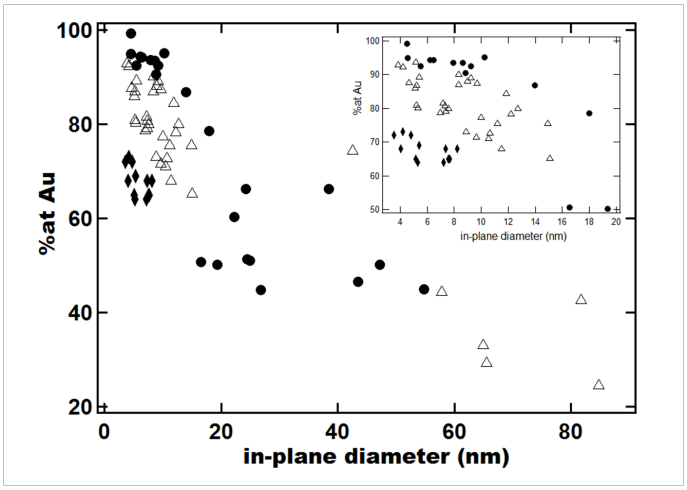

Fig. 4 The elemental composition of the NPs in sample A (△) and sample B (●). Measurements of the composition in single particles were done by STEM-EDS. In the annealed samples, the elemental composition is clearly size-dependent with an enrichment in Pd as the NPs grow in size. This composition-size dependence is due to the activation of Ostwald ripening processes. In comparison, little variation of the composition from particle to particle is observed in the as-grown sample (60-70 at.% Au). as shown by the STEM-EDS analysis of 12 as-grown NPs from the sample shown in Fig. 1a (⧫).

4 Discussions

In this study, $L1_0$ and $L1_2$ chemical orders have been stabilized in Au-Pd nanoalloys. To access the stable phase of Au-Pd alloy in the composition-temperature space, the NPs with initial completely disordered fcc structure are annealed at high-temperatures. In this work, loss of structural uniformity is a common consequence of annealing. Intriguingly, subtle changes in annealing parameters lead to drastic changes in the ordering processes that occur in Au-Pd nanoalloys during high-temperature annealing. Indeed, annealing at a temperature of 600°C for 10 hours results in a $L1_0$ order (sample A) while decreasing the annealing temperature to about 500°C leads to a $L1_2$ order after 8 hours (sample B). As it will be described in the following, this experimentally-observed tunability of the chemical order via annealing conditions can be explained on the basis of a change in the particle's composition by thermally activated mechanisms of Ostwald ripening during annealing processes.

The chemical composition of the annealed NPs from both samples were measured by single-particle X-ray analysis. As described in the ESI, the errors in composition measurements by STEM-EDS were between 1 and 3 %. To determine the size of every particle analyzed, particle size was determined precisely by acquiring a dark-field image in scanning mode prior to X-ray analysis (see Fig. 2S). The dark-field image was then analyzed with the particle size analysis tool in Digital micrograph software to yield particle size with an error of 0.4 nm. Fig. 4 displays the variation of the elemental composition of annealed NPs in samples A (△) and B (●) as a function of particle's in-plane diameter up to about 85 nm. For comparison, the elemental compositions of 12 as-grown NPs from the sample shown in Fig. 1 are also presented (⧫). The inset of Fig. 4 shows a zoom-in view of the size-composition dependence for diameter below 20 nm. In the as-grown sample, STEM-EDS measurements show that the compositions of the NPs are between 60 and 70 at.% Au and are slightly size-dependent. This size-composition dependence can result from Ostwald ripening activated during particle growth. Upon annealing at 600°C in vacuum and in parallel to particle sintering, the composition of the annealed NPs are found to vary significantly with particle size. A clear enrichment in Pd is observed as the NPs grow in size. When the diameter is lower than about 5 nm, the NPs are nearly monometallic Au structures while for diameters exceeding 50 nm, the particle's composition tends towards $\mathbf{Au_{30}Pd_{70}}$. Between these extreme compositions, the Au content decreases monotonously with size. A similar trend is obtained when analyzing sample B. However, due to the lower annealing temperature, particle sintering is less severe in this sample. Indeed, the particle size does not exceed 60 nm where the Au content is about 40 %. The simultaneous evolution of particle size and com-

position observed during high-temperature annealing can be understood by considering the processes that contribute to particle sintering.

Particle sintering in nanoalloy occurs through two main mechanisms : substrate mediated particle coalescence (static and dynamic) and Ostwald ripening process. During static coalescence, atomic diffusion takes place between immobile NPs via the support or the medium encapsulating the NPs. As for dynamic coalescence mechanism, it involves NPs that diffuse on the support and when in close interaction, merge to form bigger NPs. Coalescence mechanisms do not give rise to any variation in particle composition as sintering proceeds. As for Ostwald ripening, it is a thermoactivated process. During Ostwald ripening, large thermodynamically favorable NPs grow by taking up mobile atoms at the expense of smaller ones which shrink. In the case of an assembly of monometallic NPs, Ostwald ripening results solely in a broadening of the size distribution. When dealing with NPs made of two different metals, Ostwald ripening can lead to a size-dependent composition as shown in CoPt[36], IrPd[37] and AuPd [38,39] nanoalloys. In CoPt subject to high-temperature annealing, an enrichment in Co as the particles grow in size was observed. This compositional change has been attributed to a two-tiered Ostwald ripening mechanisms with respect to the transfer of Co and Pt atoms between particles. The evaporation rate of Co atoms from nanoparticle being higher than that of Pt atoms leads to an enrichment in Co with particle size.

Ostwald ripening in carbon-supported Au-Pd nanoclusters has been observed both at room temperature upon exposure to hydrogen gas[39] and during calcination at 400°C[38]. Hydrogen-induced Ostwald ripening occurs since in the presence of hydrogen, the binding energy of the constituent atoms of a Au-Pd NP is reduced leading to their spontaneous detachment from the NP. Since the detached Au and Pd atoms have different mobility on the TEM carbon support, the composition of the NP varies as Ostwald ripening proceeds, with the faster Pd atoms enriching the large NP. In the work of Herzing *et al* where Ostwald ripening was induced during calcination,the size-composition dependence was opposite to the one observed in the presence of hydrogen by Di Vece *et al*. Indeed, the latter showed that the Au-to-Pd ratio decreased with NP size. In the present work, Ostwald ripening is thermally induced in vacuum and the composition variations observed can be fully understood by considering the energetics of the two limiting mechanisms associated with this ripening process: detachment of the metal atoms from the clusters and diffusion of the detached atoms until they are captured by other clusters on the support. The detachment of atoms from a cluster is governed by the cohesive energy E_c of the cluster and the energy of adsorption E_a of the detached atom on the surface. The amount of energy required to detach an atom from a cluster is equal to the energy difference between its final (on the support) and initial states (in the cluster), i.e. $E_a - E_c$. Thus, to activate the evaporation of atoms from a cluster, the minimum energy required is equal to the energy barrier ($E_a - E_c$). The experimental cohesive energy per atom for bulk gold and palladium are 3.81 eV and 3.89 eV respectively[40]. It should be noted that these large values of the cohesive energy exclude re-evaporation of metal atoms in the absence of any thermal excitation. The absorption of gold and palladium atoms have been studied on graphene by first-principles calculations[41]. Estimation of adsorption energies per atom for Au and Pd adatoms on graphene are 0.10 and 1.15 eV respectively. These values leads to an evaporation barrier per atom equals to 3.71 eV and 2.74 eV for Au and Pd evaporation respectively. These energies are much higher than the diffusion barriers in noble metals which are very small with only few meV. Thus, Ostwald ripening in Au-Pd alloys is limited by the evaporation barriers which favor the detachment of Pd atoms. This preferential transfer of palladium atoms between NPs accounts for the size-composition dependence measured experimentally. The growth kinetics and evolution of composition of the annealed NPs are influenced by both the annealing conditions and the initial structure (composition, size) of the as-grown NPs.

In the sample A, a large spread out of the composition is observed in the size domain 5-20 nm (see inset of Fig. 4). For instance, for a particle diameter around 10 nm, the composition varies between 60 at.% Au and that of pure gold. From these data, we cannot exclude the presence of $L1_2$ order in sample A. Indeed, our UHRTEM measurements shows that few NPs with $L1_2$-order were present in sample A in the size range below 20 nm. In sample B, variations in composition are less significant in the size domain 5-20 nm. The Au content remains mainly between 80 and 90 at.% Au. At these compositions, the predominant order is expected to be of $L1_2$-type (the order parameter being the highest at Au_3Pd composition). This is confirmed by UHRTEM analysis (as those shown in Fig. 3) of a large number of NPs from sample B. It should be noted that few $L1_0$ NPs with sizes below 20 nm were also observed in our high-resolution measurements. The composition of these NPs should be close to the equiatomic composition at which the $L1_0$ order is highest. The formation of these NPs is again a result of the thermally-activated Oswald ripening during annealing. Finally, due to the large distribution in composition after annealing, the ordered NPs were found to coexist with large number of chemically-disordered fcc NPs in both samples A and B.

5 Conclusions

In this work, epitaxially-grown Au-Pd nanoalloys were annealed in vacuum at temperatures above 400°C for few hours (6-10 hours). The initial structure of the nanoalloys was of disordered fcc-type. After annealing, $L1_0$- and $L1_2$- chemically-

ordered monocristalline NPs were observed in the Au-rich domain of the phase diagram at temperatures between 500-600°C. Single particle X-ray analysis showed that chemical ordering occurred in parallel to a two-tiered Ostwald ripening activated during high-temperature annealing. As a result of this thermally-activated Ostwald ripening, the particle size distribution is inevitably broadened and a size-composition dependence is established upon annealing. The composition distribution of the latter is found to be highly dependent on the annealing conditions with the general trend being an enrichment in Pd as the NPs grow in size. These results constitute the first experimental evidence of the stabilization of long-range orders in Au-Pd nanoalloys. In terms of their catalytic properties, these ordered Au-Pd NPs may offer a new class of advanced nanocatalysts for various chemical reactions. However, in order to fully realize the potentials of these ordered nanostructures in heterogeneous catalysis, the detrimental effects of particle sintering at high temperatures should be limited and fully understood. Moreover, we strongly believe that both *ab initio* and semi-empirical simulations of the thermodynamic properties of Au-Pd nanoalloys would greatly benefit from the present work by providing experimental data which can be used to refine of simulation methodology.

Acknowledgements

The authors acknowledge the support of the French Agence Nationale de la Recherche (ANR) under reference ANR-11-BS10-009. We are also grateful to Région Ile-de-France for convention SESAME E1845 for the support of the JEOL ARM 200F electron microscope installed at Paris Diderot University.

References

1 M. S. Chen, D. Kumar, C. W. Yi and D. W. Goodman, *Science*, 2005, **310**, 291–293.
2 L. Kesavan, R. Tiruvalam, M. H. Ab Rahim, M. I. bin Saiman, D. I. Enache, R. L. Jenkins, N. Dimitratos, J. A. Lopez-Sanchez, S. H. Taylor, D. W. Knight, C. J. Kiely and G. J. Hutchings, *Science*, 2011, **331**, 195–199.
3 D. I. Enache, J. K. Edwards, P. Landon, B. Solsona-Espriu, A. F. Carley, A. A. Herzing, M. Watanabe, D. W. Kiely, C. J.and Knight and G. J. Hutchings, *Science*, 2006, **311**, 362–365.
4 E. N. Ntainjua, M. Piccinini, S. J. Freakley, J. C. Pritchard, J. K. Edwards, A. F. Carley and G. J. Hutchings, *Green Chemistry*, 2012, **14**, 170–181.
5 B. Coq and F. Figueras, *Journal of Molecular Catalysis A: Chemical*, 2001, **173**, 117–134.
6 D. Wang, A. Villa, F. Porta, L. Prati and D. Su, *J. Phys. Chem. C*, 2008, **112**, 8617–8622.
7 B. Pawelec, A. M. Venezia, V. La Parola, E. Cano-Serrano, J. M. Campos-Martin and J. L. G. Fierro, *Applied Surface Science*, 2005, **242**, 380–391.
8 A. M. Venezia, V. La Parola, B. Pawelec and J. L. G. Fierro, *Applied Catalysis A: General*, 2004, **264**, 43–51.
9 D. Ferrer, A. Torres-Castro, X. Gao, S. Sepulveda-Guzman, U. Ortiz-Mendez and M. Jose-Yacaman, *Nano Lett.*, 2007, **7**, 1701–1705.
10 G. Hamm, C. Becker and C. R. Henry, *Nanotechnology*, 2006, **17**, 1943–1947.
11 E. Perez-Tijerina, M. Gracia Pinilla, S. Mejia-Rosales, U. Ortiz-Mendez, A. Torres and M. Jose-Yacaman, *Faraday Discuss.*, 2008, **138**, 353–362.
12 H. Okamoto and T. B. Massalski, *Bulletin of Alloy Phase Diagrams*, 1985, **6**, 229–235.
13 A. Nagasawa, *J. Phys. Soc. Japan*, 1964, **19**, 2345–2346.
14 A. Nagasawa, Y. Matsuo and J. Kakinoki, *J. Phys. Soc. Japan*, 1965, **20**, 1881–1885.
15 Y. Matsuo, A. Nagasawa and J. Kakinoki, *J. Phys. Soc. Japan*, 1966, **21**, 2633–2637.
16 Y. Kawasaki, S. Ino and S. Ogawa, *J. Phys. Soc. Japan*, 1971, **30**, 1758–1759.
17 V. I. Iveronova and A. A. Katsnelsonsov, *Soviet Physics-Crystallography*, 1967, **11(4)**, 504–507.
18 Y. Ding, F. R. Fan, Z. Q. Tian and Z. L. Wang, *J. Am. Chem. Soc*, 2010, **132**, 12480–12486.
19 I. Atanasov and M. Hou, *Surface Science*, 2009, **603**, 2639–2651.
20 B. Shan, L. G. Wang, S. Yang, J. Hyun, N. Kapur, Y. J. Zhao, J. B. Nicholas and K. Cho, *Phys. Rev. B*, 2009, **80**, 035404.
21 S. V. Barabash, V. Blum, S. Muller and A. Zunger, *Phys. Rev. B*, 2006, **74**, 035108.
22 M. H. F. Sluiter, C. Colinet and A. Pasturel, *Phys. Rev. B*, 2006, **73**, 174204.
23 A. Brown, *Acta Crystallographica*, 1961, **14**, 856–860.
24 J. Kanamori and Y. Kakehashi, *Journal de Physique (Paris), Colloque C7*, 1977, **38**, C7–274.
25 D. Alloyeau, C. Ricolleau, C. Mottet, T. Oikawa, C. Langlois, Y. Le Bouar, N. Braidy and L. A., *Nature Materials*, 2009, **8**, 940–946.
26 C. Langlois, D. Alloyeau, Y. Le Bouar, A. Loiseau, T. Oikawa, C. Mottet and C. Ricolleau, *Faraday Discuss.*, 2008, **138**, 375–391.
27 Y. Hirotsu and K. Sato, *Journal of Ceramic Processing Research*, 2005, **6**, 236–244.
28 Y. Kohno, E. Okunishi, T. Tomita, I. Ishikawa, T. Kaneyama, Y. Ohkura, Y. Kondo and T. Isabell, *Microscopy and Analysis Supplement*, 2010, **24**, S9–S13.
29 M. Haider, S. Uhlemann, E. Schwan, H. Rose, B. Kabius and K. Urban, *Nature*, 1998, **392**, 768–769.
30 C. Ricolleau, J. Nelayah, T. Oikawa, Y. Kohno, N. Braidy, G. Wang, F. Hue, I. Florea, V. Pierron Bohnes and D. Alloyeau, *Journal of Electron Microscopy*, 2012, **62**, 283–293.
31 G. Cliff and G. W. Lorimer, *Journal of Microscopy-oxford*, 1975, **103**, 203–207.
32 K. Fukaya, S. Ino and S. Ogawa, *Transactions of the Japan Institute of Metals*, 1978, **19**, 445–453.
33 M. Gillet and A. Renou, *Surface Science*, 1979, **90**, 91–101.
34 G. Rupprechter, K. Hayek, L. Rendon and M. José-Yacamán, *Thin Solid Films*, 1995, **260**, 148–155.
35 K. Sato, J. G. Wen and J. M. Zuo, *Journal of Applied Physics*, 2009, **105**, 093509.
36 D. Alloyeau, G. Prevot, Y. Le Bouar, T. Oikawa, C. Langlois, A. Loiseau and C. Ricolleau, *Physical Review Letters*, 2010, **105**, 255901.
37 L. Piccolo, S. Nassreddine, M. Aouine, C. Ulhaq and C. Geantet, *Journal of Catalysis*, 2012, **292**, 173–180.
38 A. A. Herzing, M. Watanabe, J. K. Edwards, M. Conte, Z. R. Tang, G. J. Hutchings and C. J. Kiely, *Faraday Discussions*, 2008, **138**, 337–351.
39 M. Di Vece, S. Bals, J. Verbeeck, P. Lievens and G. Van Tendeloo, *Physical Review B*, 2009, **80**, 125420.
40 C. Kittel, *Introduction to Solid State Physics, 6th ed.*, John Wiley & Sons, New York, 1986.

41 X. Liu, C.-Z. Wang, M. Hupalo, H.-Q. Lin, K.-M. Ho and T. M. C., *Crystals*, 2013, **3**, 79–111.